IAC-18,C1,8,11,x47038

ON THE SOPHISTICATED ORBIT DESIGN OF THE LUNAR METEOROID IMPACTS OBSERVER CUBESAT

Diogene A. Dei Tos[1]

Francesco Topputo[2], Mauro Massari[3], James D. Biggs[4], Ana M. Cipriano[5]

The Earth–Moon system is constantly bombarded by meteoroids of different sizes, and their numbers are significant. The Lunar Meteoroid Impacts Observer (LUMIO) is a CubeSat mission that shall observe, quantify, and characterize the meteoroid impacts by detecting their flashes on the lunar farside. This complements the knowledge gathered by Earth-based observations of the lunar nearside, thus synthesizing a global information on the lunar meteoroid environment. A spaced-based asset improves the quality and quantity of lunar meteoroid impact flashes detection and helps initiate a Lunar Situational Awareness program. LUMIO is winner of ESA's LUCE (Lunar CubeSat for Exploration) SysNova competition, and as such it is being considered by the Agency for implementation in the near future. In this paper, an orthodox trade-off analysis is carried out for LUMIO operative orbit selection, ranging from selenocentric Keplerian orbits to periodic orbits of the Earth–Moon restricted three-body problem, and motion in a quasi-real solar system model. LUMIO is planned to be released on an elliptical quasi-polar lunar orbit. We propose the implementation of a sophisticated orbit design, concept of operations, and station-keeping strategy: LUMIO is placed on a quasi-halo orbit about Earth–Moon L_2 where permanent full-disk observation of the lunar farside is made. This prevents having background noise due to Earthshine, and thus permits obtaining high-quality scientific products. Repetitive operations are also foreseen, the orbit being in near 2:1 resonance with the Moon orbit. A large set of quasi-halo orbit is computed in the high-fidelity Roto-Pulsating Restricted n-Body Problem. LUMIO operative orbit is then selected upon minimization of station-keeping cost and transfer cost. In this work, we show a comprehensive orbit design for LUMIO and discuss possible improvements in view of the mission implementation.

1 Introduction

The Earth–Moon system is constantly bombarded by meteoroids of different sizes, and their numbers are significant. By observing the lunar surface impacts, whose flux is similar to that of the Earth, detailed information could be obtained regarding their magnitudes, velocities, temporal and spatial distributions. This information has applications in generating high-fidelity solar-system meteoroid models, validating the existing lunar impact models, contributing to lunar seismology studies and interior modeling, and initiating a Lunar Situational Awareness program for future exploration missions. The flashes produced by the lunar meteoroid impacts are currently observed from Earth-based resources, but they are restricted by geometry, illumination, and weather.

In the framework of the SysNova initiatives, under the theme of LUCE, the European Space Agency issued the following technology challenge to the scientific community: *If you could fly a CubeSat to the Moon, what could such a tiny satellite do there?* In responding to the SysNova competition, a futuristic mission to the Moon has been proposed: the LUMIO mission, placed at Earth–Moon L_2, to observe, quantify, and characterize the meteoroid impacts by detect-

ing the impact flashes on the lunar farside. This will complement the knowledge gathered by Earth-based observations of the lunar nearside, thus synthesizing a global information of the Lunar Meteoroid Environment. The mission utilizes a 12U form-factor CubeSat which carries the LUMIO-Cam, an optical instrument capable of detecting light flashes in the near-infrared and visible spectrum to continuously monitor and process the optical information.

In this paper, we address the challenges and solutions of designing a robust and versatile trajectory in cislunar space for an active platform with very limited resources (e. g., a CubeSat) while effectively performing scientific measurements. Specifically, the LUMIO baseline operative orbit is selected based on a rigorous trade-off analysis on geometric, maintenance, and reachability constraints. Orbital geometry to aid scientific observations, station-keeping (S/K), and transfer cost are considered in the analysis. The mission utilizes a novel orbit design and latest CubeSat technologies to serve as a pioneer in demonstrating how CubeSats can become a viable new tool for innovative planetary research and deep space exploration.

The remainder is organized as follows. Section 2 puts forward the scientific relevance of observing meteoroids impact with the lunar surface, while in Section 3 an overview of the LUMIO mission is given. Section 4 deals with the mission analysis, covering the design of transfer and operative phases and the concept of operations. A baseline mission is then formulated in Section 5 and critical conclusions are drawn in Section 6.

2 Lunar situational awareness

Impacts due to near-Earth objects (NEO) could cause a devastating humanitarian crisis and potentially the extinction of the human race. While the probability of such an event is low, the outcome is so

---

[1]Postdoctoral Fellow, Department of Aerospace Science and Technology, Politecnico di Milano, diogenealessandro.detos@polimi.it

[2]Assistant Professor, Department of Aerospace Science and Technology, Politecnico di Milano, Via La Masa 34, 20156, Milano, Italy; francesco.topputo@polimi.it

[3]Assistant Professor, Department of Aerospace Science and Technology, Politecnico di Milano, Via La Masa 34, 20156, Milano, Italy; mauro.massari@polimi.it

[4]Associate Professor, Department of Aerospace Science and Technology, Politecnico di Milano, Via La Masa 34, 20156, Milano, Italy; jamesdouglas.biggs@polimi.it

[5]Young Graduate Trainee, ESTEC, European Space Agency, Keplerlaan 1, 2201 AZ Noordwijk, Netherlands; ana.cipriano@esa.int

catastrophic that it is imperative to invest resources to mitigate them. Telescopic surveys detect NEO of size greater than 1 km down to 1 meter, but there are few direct methods for monitoring the sub-meter meteoroid population. Serendipitous monitoring of atmospheric explosions due to airbursts of meteoroids are being undertaken. These objects are part of the roughly 33 metric tons of debris impacting the Earth each day.

Vast amounts of meteoroids and micrometeoroids continuously enter the Earth–Moon system and consequently become a potential threat which has caused, in particular, a substantial change in the lunar surface and its properties [1]. The Moon has no atmosphere to protect itself and is subjected to impacts from meteoroids ranging from a few kilograms to tens of grams each day. Recent observations from the camera on NASA's LRO have provided direct evidence for the devastating effect of such impacts on the lunar surface [2]. Based on these observations, it is now evident that the top few centimeters of the regolith on the entire lunar surface is moved every $81,000$ years. This new finding is significant as previous models had predicted it to occur over a period of 10 million years. The constant mixing of the regolith with exogenic material (remnant impactor material) has implications for studying the lunar surface using remote sensing techniques, such as reflectance spectroscopy that sample only the top hundred microns. The high impact rate on the lunar surface also has important implications for future human and robotic assets that will inhabit the Moon for significant periods of time, and a greater understanding of these impacts is required.

A better understanding of the lunar impact situation is essential for the design and safety of future Moon bases, robotic and human exploration of the Moon. Long-term missions will require a dedicated space-based impact-monitoring asset to address the problem of weather-dependent observation quality and also to fully understand the impact of NEO on the farside of the Moon. As the meteoroids impact the lunar surface their kinetic energy is partitioned into

1. The excavation of a crater;

2. The generation of seismic waves;

3. the production of a light flash.

The seismic waves propagate through the lunar interior and can be detected by seismometers emplaced in situ. The fresh craters can be detected by taking and comparing a myriad of high-resolution images of the lunar surface. Observing the light flashes is the only viable way to detect lunar meteoroid impacts remotely. Such observations reveal characteristics like energy levels and velocities of the individual meteoroids, which are crucial for understanding and describing the meteoroid population. The number, intensities and temporal/spatial distributions of these impacts are characterized in Oberst *et al.* [1].

3 The LUMIO mission: an overview

The LUMIO mission concept is proposed to address the issues mentioned above in Section 2. Specifically,

Science Question. What are the spatial and temporal characteristics of meteoroids impacting the lunar surface?

Science Goal. Advance the understanding of how meteoroids evolve in the cislunar space by observing the flashes produced by their impacts with the lunar surface.

Science Objective. Characterize the flux of meteoroids impacting the lunar surface.

The Lunar Meteoroid Impact Observer mission concept is proposed to accomplish the scientific objective above. The LUMIO concept focuses on monitoring the lunar surface for meteoroid impacts. Performing this investigation with space-based assets yields a number of benefits, namely,

1. Observations are not biased by weather, elevating the quality of the scientific product;

2. Meteoroids impacting the lunar farside can be observed, so complementing the ground-based, lunar nearside observations;

3. Permanent, full-disk observations could be done regardless of the day/night cycle.

LUMIO is expected to be deployed into a lunar orbit by a larger Lunar Orbiter providing transportation and data relay services. The parking orbit is an ellipse with periselene altitude of 200 km, aposelene altitude between 500 and $15,000$ km, and inclination between 50 and 90 degrees over the lunar equator. The general mission architecture is shown in Figure 1, where a Earth–Moon L_2 halo is considered. The mission is divided in 6 well defined phases:

Phase 1. Pre-launch and launch;

    1-i. Starts 1 year before launch and ends after launcher successfully leaves Earth atmosphere.

Phase 2. Parking;

    2-i. Starts when the Lunar Orbiter deploys LUMIO on the prescribed selenocentric elliptic parking orbit;

    2-ii. Ends when LUMIO performs the stable manifold injection maneuver (SMIM);

    2-iii. Lasts 14 days.

Phase 3. Transfer;

    3-i. Starts when LUMIO completes the SMIM;

    3-ii. Ends when LUMIO performs the halo injection maneuver (HIM);

    3-iii. Lasts 14 days.

Phase 4. Operative;

    4-i. Starts when LUMIO completes the HIM;

    4-ii. Ends after one year of operations.

Phase 5. Extension;

    5-i. May start when LUMIO completes the operative phase, provided sufficient on-board resources are available to continue nominal operations;

    5-ii. Lasts 6 months.

Phase 6. End of Life;

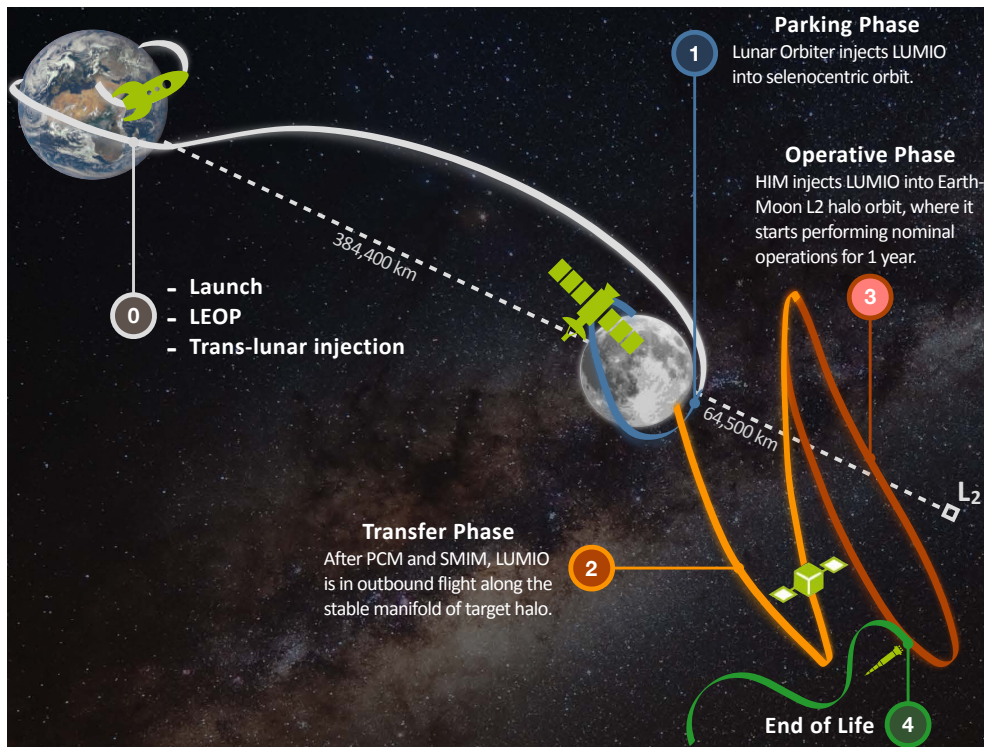   6-i. Ends when the disposal maneuver is correctly performed.

Fig. 1: General mission architecture for LUMIO.

4 LUMIO mission analysis

Three factors are accounted for the operative orbit selection trade-off of LUMIO: a) Scientific requirements and return (e. g., number of detectable impact flashes); b) Cost constraints and total Δv effort to get and stay in the final orbit (e. g., transfer maneuvers and station-keeping); and c) Autonomy of operations and the ability to navigate and acquire images without relying on the Lunar Orbiter or Earth commands (e. g., constraints on Moon disk visibility). It has been shown that remotely detecting flashes is the only technically and economically viable option for a CubeSat to monitor meteoroid impacts on the lunar surface [3]. Referring to Figure 2, a three-layer trade-off study is performed to select the orbit LUMIO employs to perform impact flashes detection:

1. A preliminary trade-off scans different orbit families to check coverage, lifetime, and accessibility characteristics of the orbit families in view of LUMIO science objective. The orbit families encompass frozen perturbed Keplerian orbits [4] and several three-body libration point orbits (LPO), i. e., halos, planar and vertical Lyapunov orbits, distant retrograde orbits, and near-rectilinear halo orbits (NRHO). Candidate families are the output of this first step [3].

2. In a second step, the physics of the impact is modeled with the space environment, the local orbital geometry, and the payload performances and parameters. This model is validated against Neliota dataset in Cipriano *et al.* [3]. Ad-hoc simulations engage the scientific requirement of maximizing the number of observable impacts with the need to have lunar full disk visibility for autonomous optical navigation in oder to produce feasible orbit families for LUMIO operative orbit selection [5].

3. Finally, a detailed trade-off quantifies and compares the station-keeping and transfer costs for each feasible orbit.
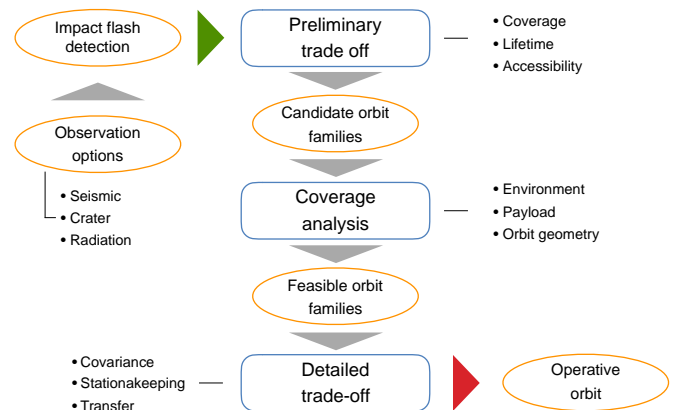

Fig. 2: Trade-off scheme for the selection of LUMIO operative orbit.

Tab. 1: Parameters of the Earth–Moon system quasi-halos.

| ID	C_j [adim]	A_z [km]	Final date [TDB]
−100001	3.1613	6973.94	2022 Feb 13 23:28:27.785
−100002	3.16	8436.02	2022 Feb 13 17:10:33.925
−100003	3.15	15172.33	2022 Feb 10 14:18:56.282
−100004	3.14	19259.07	2022 Feb 07 04:58:21.979
−100005	3.13	22225.50	2022 Feb 03 11:53:55.318
−100006	3.12	24486.23	2022 Jan 30 09:28:50.399
−100007	3.11	26220.52	2022 Jan 25 19:35:37.396
−100008	3.10	27517.73	2022 Jan 20 15:22:08.872
−100009	3.09	28418.41	2022 Jan 14 16:48:53.009
−100010	3.08	28933.50	2022 Jan 07 18:09:09.066
−100011	3.07	29041.94	2021 Dec 30 10:33:48.374
−100012	3.06	28683.38	2021 Dec 20 03:31:03.834
−100013	3.05	27725.08	2021 Dec 06 18:01:36.741
−100014	3.04	25844.92	2021 Nov 17 15:42:38.809
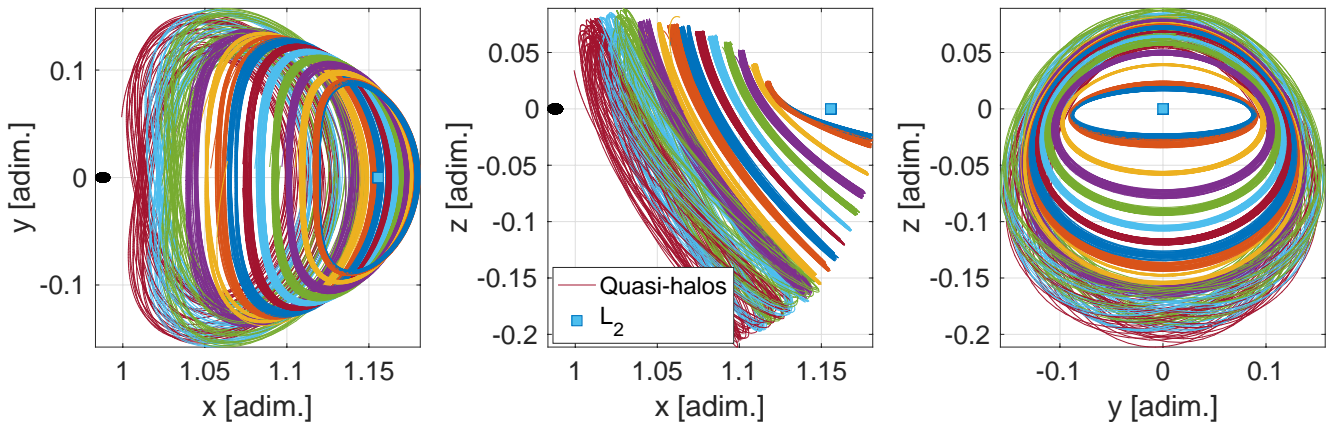
Fig. 3: Projection of Earth–Moon L_2 quasi-halos in the roto-pulsating frame. (adim. stands for nondimensional)

In this work, the focus is placed on the last step of the analysis to select a LUMIO operative orbit. LUMIO operative orbit is selected upon the criteria mentioned above. When considering also flight heritage, e. g., technology readiness level (TRL), and solar eclipse occurrences, the sole feasible orbit family is the Earth–Moon L_2 halo family. The methodology described in [6] is employed to find a set of quasi-periodic halo orbits (sometimes referred here as quasi-halos or quasi-halo orbits) about Earth–Moon L_2. Fourteen quasi-halo orbits are computed in the high-fidelity roto-pulsating restricted n-body problem (RPRnBP) and saved as SPICE[1] kernels. The initial feeds to compute the quasi-halo samples are Earth–Moon three-body halos at 14 different Jacobi constants, ranging from $C_j = 3.04$ to $C_j = 3.1613263$. Table 1 shows the quasi-halos nondimensional Jacobi energies and the relevant information to use the associated SPICE kernels. All orbits are computed starting from 2020 August 30 00:00:00.000 TDB (dynamical barycentric time). Although quasi-halos, shown in Figure 3 in the roto-pulsating frame (RPF), are computed for a fixed initial epoch, the persistence of libration point orbits in the solar system ephemeris model allows freedom in the refinement algorithm also for mission starting at different epochs [6].

Quasi-halo orbits of Figure 3 are possible LUMIO operative orbits. As the orbit becomes more energetic, or as its Jacobi constant decreases, the quasi-halo exhibits a wider range of motion both in terms of Moon range and of geometrical flight envelope about the corresponding circular restricted three-body problem (CRTBP) trajectory. The latter trend is disadvantageous when a hard pointing constraint must be respected. On the other hand, the lunar distance places a constraint on the minimum field of view (FOV) for the optical instrument on board LUMIO to be able to resolve the Moon full disk at any location along the quasi-halo. Bar charts of Figure 4 show the ranges from the lunar surface to the quasi-halo samples. For discrete values of the camera field of view, simple trigonometric calculations provide the minimum distance for which the optical instrument is able to resolve the full disk of the Moon. The wider the FOV, the closer LUMIO can get to the Moon still being able to see its full disk. The horizontal lines in Figure 4 indicate this distance for different values of FOV.

---

[1]SPICE is NASA's Observation Geometry and Information System for Space Science Missions [7], [8]. The toolkit is freely available through the NASA NAIF website http://naif.jpl.nasa.gov/naif/. Last downloaded on February 7, 2018.
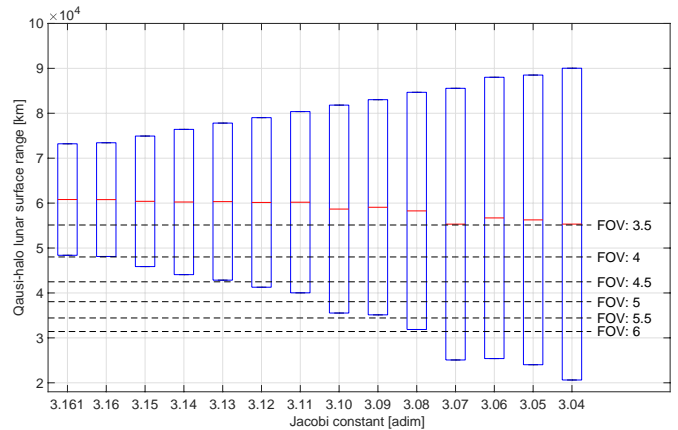

Fig. 4: Bars for quasi-halos ranges to lunar surface. (FOV in degrees)

4.1 CONCEPT OF OPERATIONS

In the CRTBP, the libration points are at rest with respect to a frame co-rotating with the smaller and larger primaries. Consequently, a halo orbiting the Earth–Moon L_2 always faces the lunar farside. On top of this, for a wide range of Jacobi energies, Earth–Moon L_2 halos are almost locked into a 2:1 resonance, that is 2 orbital revolutions
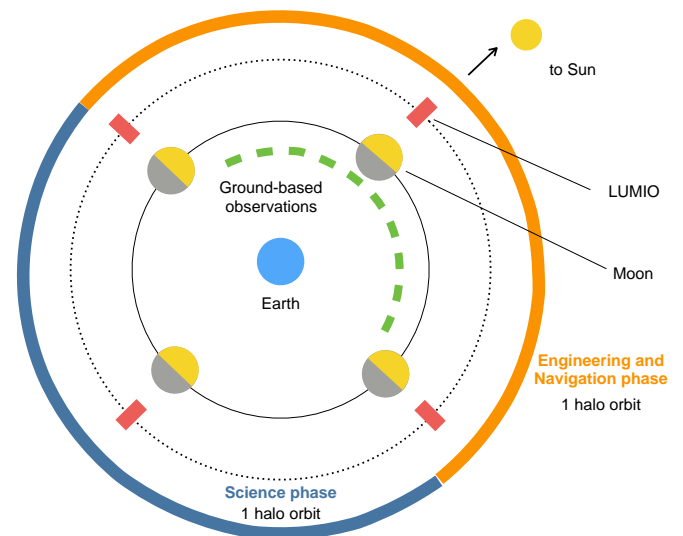

Fig. 5: LUMIO concept of operations.

in 1 synodic period. The sun completes a full revolution around the Moon in one synodic period, approximately $T_\text{syn} = 29.4873$ days. The synodic period is slightly larger than the lunar orbital period around Earth to account for the amount the sun has moved along its orbit in this duration.

The quasi-resonance locking, which is also preserved in the full ephemeris quasi-halos, enables LUMIO operations to be repetitive and regular. Within the operative phase, each synodic month LUMIO moves along a) a *Science orbit* (dark solid line in Figure 5) and b) a *Navigation and Engineering orbit* (light colored solid line in Figure 5). During the Science orbit, lasting roughly 14 days, the Moon farside has optimal illumination conditions to perform flash observations (i. e., at least half lunar disk is dark). On the other hand, during the Nav&Eng orbit the Moon farside illumination conditions are apt to optical navigation routines. LUMIO concept of operations (ConOps) is somewhat simplified and tight to both resonance mechanisms and illumination conditions to properly enable scientific or other operations.

4.2 STATION-KEEPING STRATEGY

One of the main goals of the mission analysis and trajectory design process is the determination of the nominal path. In most cases, it is not strictly necessary for the spacecraft to move precisely along the nominal trajectory in order to accomplish mission objectives. Indeed, once the nominal orbit is determined, it is desired to maintain the actual flown trajectory of the spacecraft within some region (e. g., torus- or box-shaped) about the reference path. Nonmodeled perturbations and errors will cause the spacecraft to drift from the nominal path, and the unstable nature of the libration point orbits will further amplify the deviation. Assuming discrete and impulsive corrections [9], the problem consists in finding the required corrective maneuvers in terms of magnitude, direction, and timing of each Δv. In optimal S/K problems, the total Δv budget is minimized.

In light of the limited Δv capability, fuel consumption for S/K around the operative orbits will be a critical factor for mission sustainability. Using the generated orbits as reference trajectories, a computationally efficient Monte-Carlo routine is devised for estimation of the cost of each S/K maneuver. An effort is directed toward the development of a S/K strategy that can be used to maintain CubeSats near such nominal libration point trajectories. Specifically, the S/K cost is estimated by employing the target points method (TPM) first introduced by Dwivedi in the case of deterministic optimal maneuver strategy for multi-target missions [10], then adapted to the problem of LPOs S/K by Howell and Pernicka [11], and finally used for JAXA's EQUULEUS mission analysis [12]. A massive Monte-Carlo simulation is performed with $10,000$ samples, considering the impact of the injection, tracking, and maneuver execution processes on the nominal orbit determined in the presence of solar radiation pressure and gravity of the main solar system celestial bodies (i. e., sun, 8 planets, the Moon, and Pluto). To precisely simulate a realistic spacecraft trajectory,

1. The initial conditions of the quasi-halos are altered to account for orbit insertion error.

2. Tracking windows are considered in which orbit determination (OD) campaigns modify the actual knowledge of the spacecraft state by means of optical measurements and non-linear filtering. Because of various uncertainties in the OD process, the
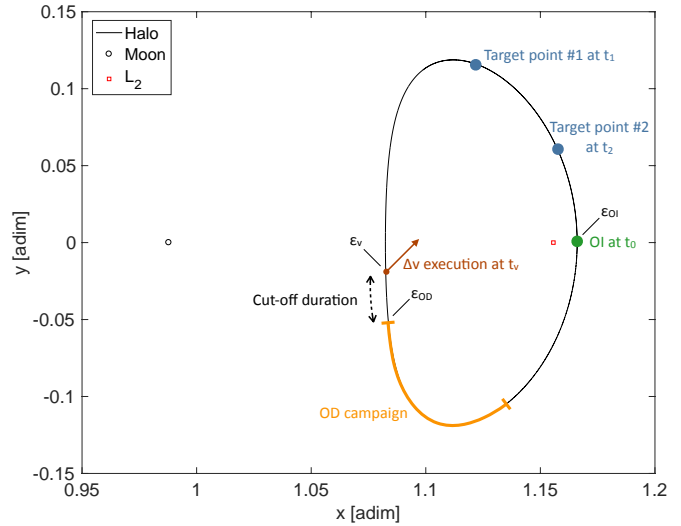

Fig. 6: Overview of S/K and TPM.

spacecraft position and velocity are never exactly known. To simulate tracking errors, the six S/C states are altered at the end of each OD campaign.

3. At various time along the trajectory, the S/K strategy will determine that a maneuver is required, and its magnitude and direction will be computed. To model the inaccuracy of maneuvers actual implementation, each $\Delta\boldsymbol{v}_{S/K}$ component is randomly altered.

The orbit injection (OI), $\boldsymbol{\varepsilon}_{OI}$, orbit determination, $\boldsymbol{\varepsilon}_{OD}$, and the maneuver execution, $\boldsymbol{\varepsilon}_{EX}$, errors are all modeled and generated with zero-mean Gaussian distributions, i. e., $\boldsymbol{\varepsilon}_{OI} \sim \mathcal{N}(0, \sigma_{OI}^2)$, $\boldsymbol{\varepsilon}_{OD} \sim \mathcal{N}(0, \sigma_{OD}^2)$, $\boldsymbol{\varepsilon}_{EX} \sim \mathcal{N}(0, \sigma_v^2)$, where σ_{OI}^2, σ_{OD}^2, σ_{EX}^2 are the covariances of the orbit insertion, orbit determination, and maneuver execution uncertainties, respectively.

The S/K maneuvers, $\Delta\boldsymbol{v}_{S/K}$, are conducted at specific selected epochs during the mission. That is, maneuver timings are parameters of the S/K strategy, rather than variables. Referring to Figure 6, every OD campaign is always terminated Δt_c time units before the maneuver execution. Δt_c is termed cut-off duration and it is necessary to compute, schedule, and prepare the maneuver. The S/K maneuver planning is assumed to use N_{tp} downstream points, i. e., the target points, as reference states to compute the maneuver magnitude and direction. In Figure 6, there are two target points, $N_{tp} = 2$, and one S/K maneuver per halo orbit. The algorithm for the detailed S/K cost analysis is shown in Algorithm 1.

4.2.1 Target points method

The TPM provides optimal $\Delta\boldsymbol{v}_{S/K}$ computed as solution of a linear-quadratic regulator (LQR) problem that minimizes a weighted sum of the maneuvers cost and the position deviation from a reference trajectory at N_{pt} downstream control points, i. e., the target points. The cost function is

$$J_{S/K} = \Delta\boldsymbol{v}_{S/K}^\text{T} Q \Delta\boldsymbol{v}_{S/K} + \sum_{i=1}^{N_{pt}} \boldsymbol{d}_i^\text{T} R_i \boldsymbol{d}_i, \qquad (1)$$

where $\Delta\boldsymbol{v}_{S/K}$ is the S/K maneuver, Q the cost weight matrix, $\boldsymbol{d}_i$ the predicted position deviation from the reference trajectory at the i-th target point, and R_i the weighing matrix of the deviation at the i-th

---

Algorithm 1 Cost estimation for of S/K along a reference quasi-halo.

1: **function** DVSK(t_0, t_f, Φ, Δt_v, Δt_c, Δt_i, σ_{OI}^2, σ_{OD}^2, σ_{EX}^2, Q, R)
2: $\quad$ $t \leftarrow t_0$
3: $\quad$ Generate six-dimensional OI error, $\varepsilon_{OI} \sim \mathcal{N}(0, \sigma_{OI}^2)$
4: $\quad$ OI: $\delta \boldsymbol{x}_\text{true} \leftarrow \varepsilon_{OI}$
5: $\quad$ **while** $t \leq t_f$ & $\delta \boldsymbol{x}_\text{true}$ **do**
6: $\quad\quad$ $t_v \leftarrow t + \Delta t_v$
7: $\quad\quad$ $t_c \leftarrow t_v - \Delta t_c$
8: $\quad\quad$ $t_i \leftarrow t + \Delta t_i$
9: $\quad\quad$ $\delta \boldsymbol{x}_\text{true} \leftarrow \Phi(t, t_c) \delta \boldsymbol{x}_\text{true}$
10: $\quad\quad$ Generate six-dimensional OD error, $\varepsilon_{OD} \sim \mathcal{N}(0, \sigma_{OD}^2)$
11: $\quad\quad$ OD: $\delta \boldsymbol{x}_c \leftarrow \delta \boldsymbol{x}_\text{true} + \varepsilon_{OD}$, where $\delta \boldsymbol{x}_c = [\delta \boldsymbol{r}_c; \delta \boldsymbol{v}_c]$
12: $\quad\quad$ Maneuver planning: $\Delta \boldsymbol{v}_{S/K} = A \sum_{i=1}^{N_{pt}} (\alpha_i \delta \boldsymbol{r}_c + \beta_i \delta \boldsymbol{v}_c)$ $\quad\quad$ ▷ See Eq. (3)
13: $\quad\quad$ $\delta \boldsymbol{x}_\text{true} \leftarrow \Phi(t_c, t_v) \delta \boldsymbol{x}_c$
14: $\quad\quad$ Generate three-dimensional maneuver execution error, $\varepsilon_{EX} \sim \mathcal{N}(0, \sigma_{EX}^2)$
15: $\quad\quad$ $\Delta \boldsymbol{v} \leftarrow \Delta \boldsymbol{v} + \Delta \boldsymbol{v} \circ \varepsilon_v$ $\quad\quad$ ▷ Here, ∘ represents the Hadamard product
16: $\quad\quad$ Maneuver execution: $\delta \boldsymbol{x}_\text{true} \leftarrow \delta \boldsymbol{x}_\text{true} + [0_{3 \times 3}; \Delta v]$
17: $\quad\quad$ $t \leftarrow t_v$
18: $\quad$ **end while**
19: **end function**

---

target point. The position deviation is predicted by means of the state transition matrix of the reference trajectory, Φ:

$$\boldsymbol{d}_i = \Phi_{rr}(t_c, t_i)\delta \boldsymbol{r}_c + \Phi_{rv}(t_c, t_i)\delta \boldsymbol{v}_c + \Phi_{rv}(t_v, t_i)\Delta \boldsymbol{v}_{S/K}. \quad (2)$$

In Eq. (2), Φ_{rr} and Φ_{rv} are 3-by-3 matrices that map deviation of position and velocity, respectively, to a position deviation at a subsequent epoch, t_c is the cut-off epoch, t_v is the maneuver execution epoch, and t_i the epoch of the i-th target point. The solution of the minimization problem yields the analytic expression for the optimal S/K maneuver:

$$\Delta \boldsymbol{v}_S/K = A \sum_{i=1}^{N_{pt}} (\alpha_i \delta \boldsymbol{r}_c + \beta_i \delta \boldsymbol{v}_c);$$

$$A = - \left[\left(Q^\text{T} + Q\right) + \sum_{i=1}^{N_{pt}} \Phi_{rv}^\text{T}(t_v, t_i) \left(R_i^\text{T} + R_i\right) \Phi_{rv}(t_v, t_i) \right]^{-1},$$

$$\alpha_i = \Phi_{rv}^\text{T}(t_v, t_i) \left(R_i^\text{T} + R_i\right) \Phi_{rr}(t_c, t_i),$$

$$\beta_i = \Phi_{rv}^\text{T}(t_v, t_i) \left(R_i^\text{T} + R_i\right) \Phi_{rv}(t_c, t_i).$$

$$(3)$$

4.2.2 Station-keeping results

Table 2 reports the standard deviations of orbit insertion, navigation, and maneuver execution errors for the S/K analysis. The values of Table 2 are in well accordane with existing applications, e. g., Artemis [13]. More important, simulations have shown the standard deviations of Table 2 can be achieved with the autonomous optical navigation algorithm on-board LUMIO [5]. All parameters for the correct functioning of Algorithm 1 have been fine-tuned with extensive simulation campaigns. The parameters fine-tuned values of the S/K algorithm are shown in Table 3. The cut-off duration of 12 hours is at the same time sufficiently short to prevent the spacecraft state knowledge from excessive growing, and long enough to schedule

maneuver execution operations on-board LUMIO. The target points are located at 35 and 42 days after orbit insertion and any subsequent S/K maneuvers. Such distant target points ensure approximately one month of quasi-halo tracking in case of maneuver execution failure. Finally, having the eigenspectrum of Q a larger magnitude than that of R_i means the optimization weighs the deviation with respect to reference position more than the $\Delta \boldsymbol{v}_{S/K}$ cost.

Figure 7 shows the strategy employed for S/K maneuvers timing. For clarity, 70 days of operations are shown and the quasi-halo orbital period is assumed to be fixed and equal to 14 days. The first quasi-halo orbit is entirely dedicated to recover any OI errors by means of two maneuvers (1 and 7 days after OI). In the orbits after that, nominal operations occur, i. e., there is a series of Nav&Eng and Science orbits. Three S/K maneuvers are placed within the Nav&Eng orbit: the first at the entry point, the second in the middle (i. e., 7 days after the entry), and the third at the end of the Nav&Eng orbit. This maneuvers frequency configuration allows for pristine Science orbit operations, albeit it increases the cost when compared to a more spread and regular distribution of S/K maneuvers.

S/K cost is computed for one year of life cycle for each of the quasi-halos in Table 1. To obtain reliable S/K cost estimation results, a massive Monte-Carlo simulation of 10, 000 cases is performed with respect to each reference orbit generated. Each Monte-Carlo run employs Algorithm 1 to compute S/K cost for a realization of ε_{OI}, ε_{OD}, and ε_{EX}. Table 4 displays the 1-year S/K cost with 1σ, 2σ, and 3σ confidence. The Monte-Carlo data is fitted by means of an Inverse Gaussian distribution. Figure 8 shows mean values with associated standard deviations (displayed as error bars) of the 1-year S/K cost. As expected, the S/K cost increases for smaller (i. e., higher Jacobi constant) quasi-halos. This trend reflects the stability (eigenspectrum of monodromy matrix) properties of halo orbits. That is, a larger halo is generally more stable and cheaper to maintain. Finally, Figure 9 shows the cumulative distribution function (CDF) for the specific case of quasi-halo of ID -100009. Clearly, the Inverse Gaussian distribution well fits the raw data, results of the Monte-Carlo simulation for the yearly $\Delta \boldsymbol{v}_{S/K}$ cost.

Tab. 2: Modeled standard deviations.

Standard deviation	LUMIO	Units
$\sigma_{OI_x}, \sigma_{OI_y}, \sigma_{OI_z}$	10, 10, 10	[km]
$\sigma_{OI_u}, \sigma_{OI_v}, \sigma_{OI_w}$	10, 10, 10	[cm/s]
$\sigma_{OD_x}, \sigma_{OD_y}, \sigma_{OD_z}$	10, 10, 10	[km]
$\sigma_{OD_u}, \sigma_{OD_v}, \sigma_{OD_w}$	10, 10, 10	[cm/s]
$\sigma_{EX_u}, \sigma_{EX_v}, \sigma_{EX_w}$	2, 2, 2	[%]

Tab. 3: Parameters of S/K analysis.

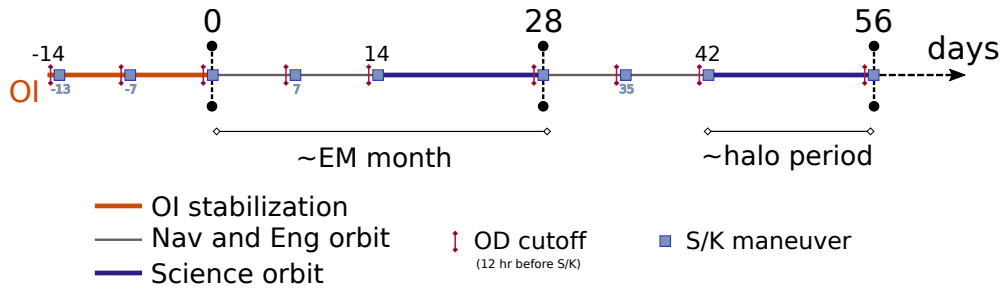| Parameter	Value	Units
Δt_c	12	[hr]
Δt_1	35	[days]
Δt_2	42	[days]
Q	$I_{3 \times 3} \cdot 10^{-1}$	[-]
R_1	$I_{3 \times 3} \cdot 10^{-2}$	[-]
R_2	$I_{3 \times 3} \cdot 10^{-2}$	[-]

Fig. 7: Strategy for station-keeping maneuvers timing.

Tab. 4: Confidence for the 1-year station-keeping cost.

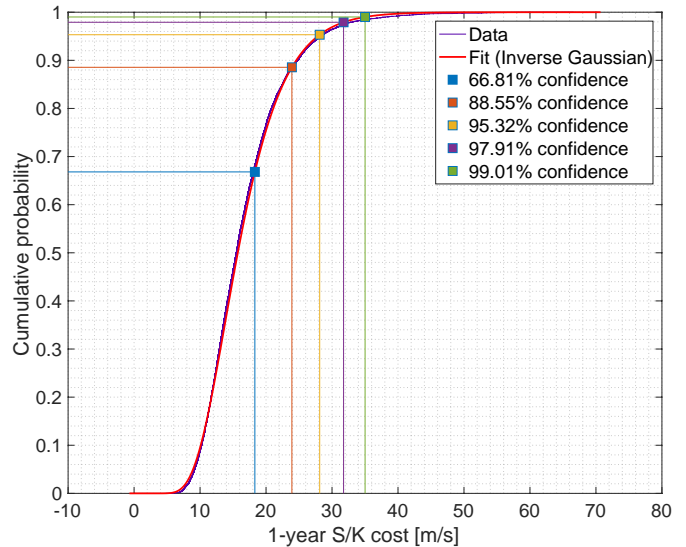| C_j [adim]	S/K cost [m/s]		
	1σ	2σ	3σ
3.16132363	75.5	137.9	196.5
3.16	72.4	131.6	186.9
3.15	53.4	92.7	128.4
3.14	40.1	66.4	89.7
3.13	29.2	45.4	59.2
3.12	22.0	31.6	39.1
3.11	17.8	23.8	28.5
3.10	13.3	16.9	19.6
3.09	18.3	23.9	28.1
3.08	11.0	13.9	15.6
3.07	8.8	10.2	11.2
3.06	8.5	9.9	10.9
3.05	7.6	8.6	9.3
3.04	7.2	7.9	8.4

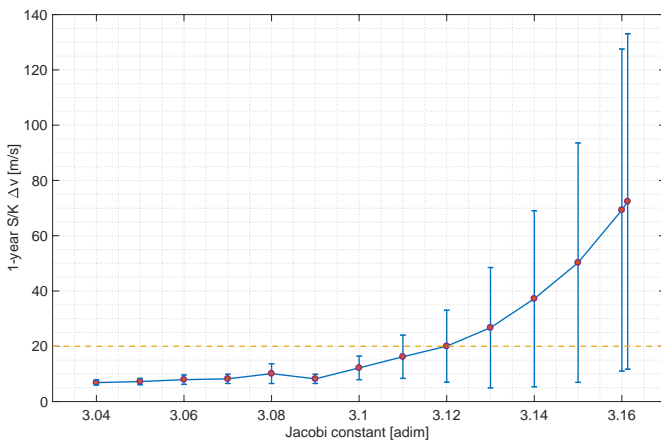Fig. 9: Station-keeping yearly cost CDF for quasi-halo -100009.

Fig. 8: Yearly station-keeping cost for set of quasi-halos.

4.3 TRANSFER PHASE DESIGN

The transfer phase of LUMIO is done in the CRTBP. Free transport mechanisms are leveraged to reach the target halo. Specifically, intersection in the configuration space is sought between the halo stable manifolds and a selenocentric transition orbit. Since the sought intersection occurs only in configuration space, a maneuver is necessary for orbital continuity. This maneuver places the spacecraft on the stable manifold of the target halo and is thus called SMIM, $\Delta\boldsymbol{v}_{\text{SMIM}}$. The Sysnova challenge provides assumptions and constraints on the system overall architecture. In particular, LUMIO shall be injected into a lunar orbit with constraints on the orbital elements shown in Table 5. For compliance with these requirements on the lunar orbiter stage, a plane change maneuver is scheduled to occur at the apocenter

of the parking orbit. The maneuver rotates the parking orbit into the transition orbit. The transfer phase starts when the plane change maneuver, $\Delta\boldsymbol{v}_{\text{pc}}$, occurs, and ends after the HIM, $\Delta\boldsymbol{v}_{\text{HIM}}$, inserts the S/C into the target halo orbit. The aim of the transfer design analysis is to find the parameters of the selenocentric transition orbit and the stable manifold that lead to a minimum $\Delta\boldsymbol{v}_{\text{SMIM}}$ at the intersection. The optimization problem is stated hereafter, and it is solved with a nonlinear programming (NLP) method.

For this analysis, it is convenient to recall the methodology used to numerically compute the invariant manifolds in the CRTBP. This approach relies on finding a linear approximation of the manifold in the neighborhood of an orbit. An algorithm is implemented that scans the stable manifold space by varying the time along the originating halo, t_{po}, and the time along the stable manifold, t_{sm}. Once t_{po} and t_{sm} are specified, the stable manifold is completely determined [14]. t_{po} uniquely specifies a state along the halo, $\boldsymbol{x}(t_{\text{po}})$. At $\boldsymbol{x}(t_{\text{po}})$, the invariant manifolds are locally spanned by the stable and unstable eigenvectors of $M(t_{\text{po}})$, the monodromy matrix associated to $\boldsymbol{x}(t_{\text{po}})$. That is, the STM evaluated over one period

Tab. 5: Orbital elements constraints.

Orbital element	Unit	Minimum value	Maximum value
h_p	[km]	200	
h_a	[km]	500	15,000
i	[deg]	50	90

of the orbit. The initial conditions used to compute the stable manifold are $\boldsymbol{x}_{s_0} = \boldsymbol{x}(t_{\text{po}}) \pm \varepsilon \boldsymbol{v}_s$, where $\boldsymbol{v}_s$ is the stable eigenvector of $M(t_{\text{po}})$ and ε is a small displacement perturbing in the stable direction, whereas the $\pm$ discriminates which of the two branches of the manifold has to be generated. As for ε, it should be small enough to preserve the local validity of the linear approximation, but also large enough to prevent from long integration times needed to compute the manifold. Here, $\varepsilon = 10^{-6}$ is used, consistently with the arguments in Gómez *et al.* [15]. t_{sm} is the duration $\boldsymbol{x}_s$ is flown in backward time. The stable manifold state yields:

$$\boldsymbol{x}_s = \boldsymbol{\varphi}(\boldsymbol{x}_{s_0}, 0; -t_{\text{sm}}), \tag{4}$$

where $\boldsymbol{\varphi}$ is the flow of the CRTBP from $\boldsymbol{x}_{s_0}$ to $-t_{\text{sm}}$. An outline of the transfer design algorithm is shown in Algorithm 2.

Algorithm 2 Transfer design.

---

procedure INITIALIZATION
    Set the CRTBP as default dynamical model
    Select C_j of target halo orbit
    Select manifold branch flying towards the Moon (i. e., left branch for L_2 LPO)
end procedure
procedure MANIFOLD SCAN FOR INITIAL GUESS GENERATION
    Set bounds for the time along the target halo, $t_{\text{po}} \in [0, T]$
    Set maximum time along the stable manifold, $t_{\text{sm}}^{(\max)}$
    Discretize t_{po} by dt_{po} to get n_t discrete values
    Initialize vector $\boldsymbol{\tau} \in \mathbb{R}^{n_t \times 3}$
    for $t_{\text{po}} = 0 \to T$ by dt_{po} with index k **do**
        Get stable manifold state, $\boldsymbol{x}_s$, for current t_{po} and $t_{\text{sm}}^{(\max)}$ ▷ See Eq. (4)
        Find t_{sm} at which altitude, $h_p = \|\boldsymbol{r}_s(t_{\text{sm}}) - \boldsymbol{r}_2\| - R_{\mathbb{C}}$, is closest to 200 km
        Store $(t_{\text{po}}, t_{\text{sm}}, h_p)$ in the k-th row of vector $\boldsymbol{\tau}$
    end for
end procedure
procedure TRANSFER MANEUVER
    Initialize vector $\boldsymbol{\Gamma} \in \mathbb{R}^{n_t \times 16}$
    loop in $\boldsymbol{\tau}$ with index j
        repeat
            Randomly initialize transition orbit elements in $\boldsymbol{e} = (h_a, i, \Omega, \omega, \theta)$
            Solve for $\Delta\boldsymbol{v}_{\text{SMIM}}$ using $\boldsymbol{e}$ and j-th row of $\boldsymbol{\tau}$ as first guess ▷ Eq. (8)
        until convergence is attained
        if $i^{(\text{opt})} \notin [50°, 90°]$ **then**
            Select nearest target inclination of parking orbit, i_{pk} ▷ see Table 5
            Schedule plane rotation around apoaxis by $\Delta i = |i_{pk} - i^{(\text{opt})}|$
            Compute plane rotation maneuver at apoaxis, $\Delta\boldsymbol{v}_{\text{pc}}$
            Compute updated Ω_{pk} and ω_{pk} of parking orbit
        else
            Set $\Delta\boldsymbol{v}_{pc} = \boldsymbol{0}$
            Set parking orbits elements equal to transition orbit elements
        end if
        Store optimization results, $(\Delta\boldsymbol{v}_{\text{SMIM}}, \Delta\boldsymbol{v}_{\text{pc}}, \boldsymbol{y}^{(\text{opt})}, \Omega_{pk}, \omega_{pk})$, in $\boldsymbol{\Gamma}$ j-th row
    end loop
end procedure

Variables. The NLP variables, collected in vector $\boldsymbol{y}$, are the Keplerian elements of the transition parking orbit and the times necessary to determine the stable manifold:

$$\boldsymbol{y} = (h_p, h_a, i, \Omega, \omega, \theta, t_{\text{po}}, t_{\text{sm}}). \tag{5}$$

Cost function. A relevant parameter representing space mission cost is the total Δv consumption:

$$J(\boldsymbol{y}) = \|\Delta\boldsymbol{v}_{\text{SMIM}}\|. \tag{6}$$

The costs associated to $\Delta\boldsymbol{v}_{\text{HIM}}$ and $\Delta\boldsymbol{v}_{\text{pc}}$ are not included in the objective function because they depend solely on the deviation between the asymptotic motion of the stable manifold, i. e., ε.

Constraints. The intersection in configuration space between the transition orbit and the stable manifold of the target halo is the most important constraint. Equality and inequality constraints are:

$$\boldsymbol{c}_{eq} = \begin{pmatrix} \boldsymbol{r}_t - \boldsymbol{r}_{\text{sm}} \\ h_p - 200 \end{pmatrix}, \qquad \boldsymbol{c} = \begin{pmatrix} 500 - h_a \\ h_a - 15,000 \end{pmatrix}, \tag{7}$$

where $\boldsymbol{r}_t$ and $\boldsymbol{r}_{\text{sm}}$ are the positions along the transition orbit and the stable manifold at the SMIM epoch, t_{SMIM}, respectively.

Statement of the problem. The problem of transfer design with an optimal impulsive maneuver can be formally stated as a constrained minimization:

$$\min_{\boldsymbol{y}} J(\boldsymbol{y}) \quad s.t. \quad \begin{cases} \boldsymbol{c}_{eq} & = \boldsymbol{0}, \\ \boldsymbol{c} & \leq \boldsymbol{0}. \end{cases} \tag{8}$$

The minimization is solved with an active-set algorithm.

4.3.1 Results of the transfer design

Algorithm 2 is applied to all halos in the Jacobi energy range of Table 1. Figure 10 shows the total transfer cost for different halos. The cost includes S/K, SMIM, and plane change maneuvers. On the other hand, Figure 11 displays four sample stable manifolds of the halo with $C_j = 3.09$ at $t_{\text{po}} = 0$ (Figure 11a), $t_{\text{po}} = T/5$ (Figure 11b), $t_{\text{po}} = 7T/10$ (Figure 11c), and $t_{\text{po}} = 9T/10$ (Figure 11d). The selection quasi-halo ID -100009 as LUMIO operative orbit is made based on results summarized in Figure 10. Indeed, quasi-halo ID -100009 is located at the center of a minimum plateau for total transfer cost which provide both a) optimality of maneuvers cost, and b) robustness against errors in the actual energy level of the injected stable manifold.

It is conjectured the reason why the transfer cost has a clearcut minimum area is twofold. 1) For high energy levels (i. e., low Jacobi constant), the stable manifold configuration space does not get close enough to the Moon to permit intersection with the selenocentric transition orbit. At the other end of the spectrum, 2) for high Jacobi constant values, the stable manifolds cross the lunar region sufficiently close to provide patching opportunities with a selenocentric transition orbit, but the speed mismatch is comparatively large. I. e., the outbound stable manifold is much faster than the S/C at periselene. The optimal transfer parameters are shown in Table 6. As expected, the SMIM occurs at the pericenter of the transition orbit. The inclination of the transition orbit already lies within the parking orbit bounds, and no plane maneuver is necessary.
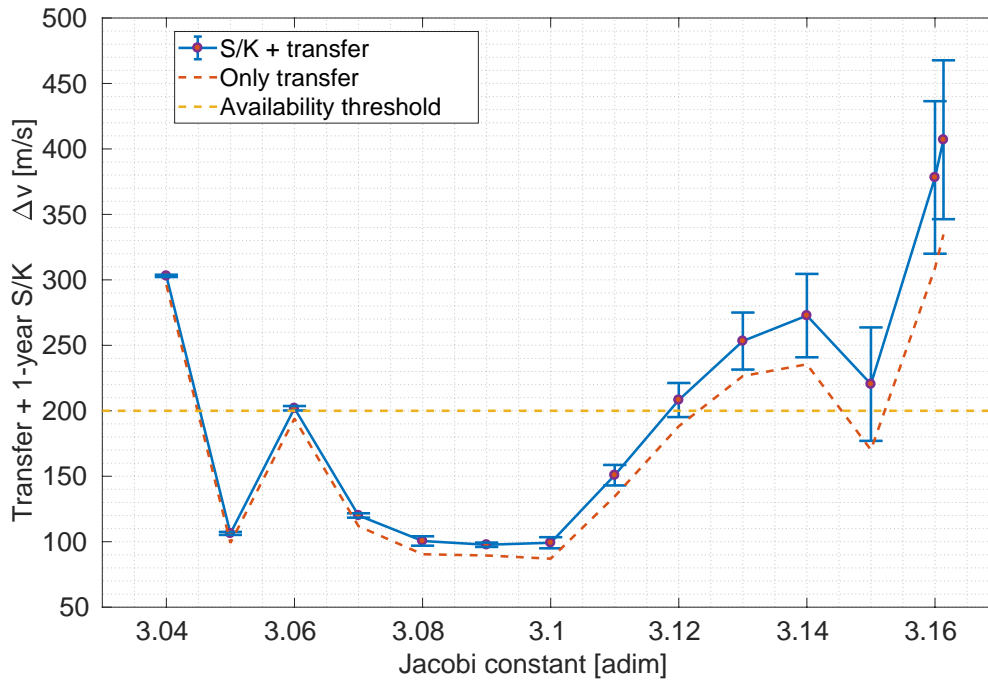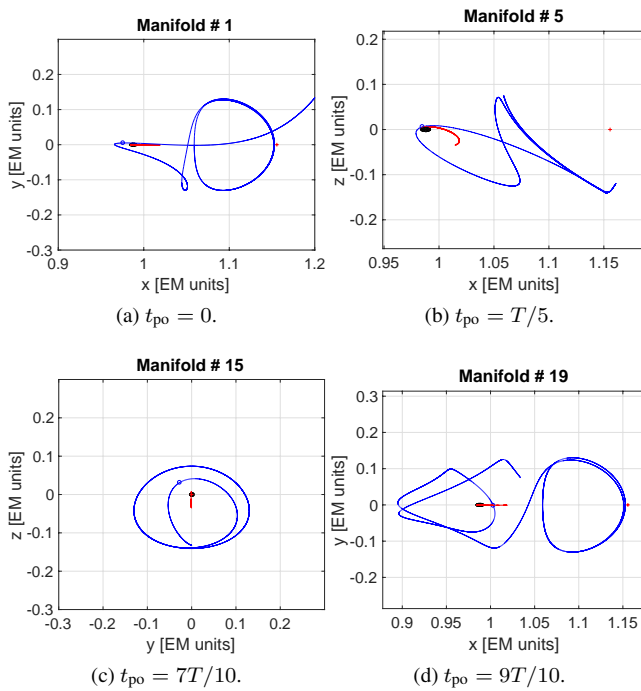
Fig. 10: Total transfer cost for different halos.

(a) $t_{\text{po}} = 0.$

(b) $t_{\text{po}} = T/5.$

(c) $t_{\text{po}} = 7T/10.$

(d) $t_{\text{po}} = 9T/10.$

Fig. 11: Stable manifolds of operative halo at different t_{po}.

Tab. 6: Main parameters for the transfer phase.

Parameter	h_a	a	e	i	Ω
Value	14964.2	9319.2	0.7921	78.1	30.0
Units	[km]	[km]	[-]	[deg]	[deg]

Parameter	ω	ϑ	T	t_{po}	t_{sm}
Value	301.2	≈ 0	22.425	0.7406	7.5397
Units	[deg]	[deg]	[hours]	[adim]	[adim]

4.4 TRAJECTORY CORRECTION MANEUVERS

A number of trajectory correction maneuvers (TCM) is scheduled to occur during the transfer along the stable manifold. In this work, the timing and the number of TCM is fixed. In particular, two TCM are scheduled, the first one day after the SMIM, and the second 7 days after Δv_{SMIM}, or equivalently 6 days after TCM1. A detailed study of the TCM problem for several LPO, just by using simple dynamical systems concepts, has shown that two TCM provide sufficient degrees of freedom [16].

In this work, the TCM are found using optimal control theory [17]. The total TCM cost, $J = \|\Delta v_{\text{TCM1}}\| + \|\Delta v_{\text{TCM2}}\|$, is minimized such that the state dispersion at the halo injection epoch is within 1000 km in position and 1 m/s in velocity. The dispersion is triggered by a bias in the stable manifold injection point, that may represent, for instance, thrust misalignment in the execution of the SMIM and/or orbit determination uncertainties. A Monte-Carlo simulation is run with 10,000 random initializations of the bias error, with zero-mean Gaussian distribution, after the SMIM is performed. During each Monte-Carlo run, an optimal problem is solved for the magnitudes and directions of Δv_{TCM1} and Δv_{TCM2}.

Table 7 shows the TCM costs with 1σ, 2σ, and 3σ confidence, for the transfer towards halo ID -100009. Monte-Carlo output data has been fit to match a Burr-type probability distribution function (PDF). The probability distribution functions of TCM1 and TCM2 are shown in Figure 12a and Figure 12c, respectively, while the cumulative distribution functions of TCM1,2 are shown in Figure 12b

Tab. 7: TCM confidence.

TCM	$\|\Delta v_{\text{TCM}}\|$ [m/s]		
	1σ	2σ	3σ
TCM1	28.6	53.0	73.1
TCM2	6.5	15.0	24.8

(a) PDF of TCM1.

(b) CDF of TCM1.

(c) PDF of TCM2.

(d) CDF of TCM2.

(e) Position confidence ellipsoid at HIM.

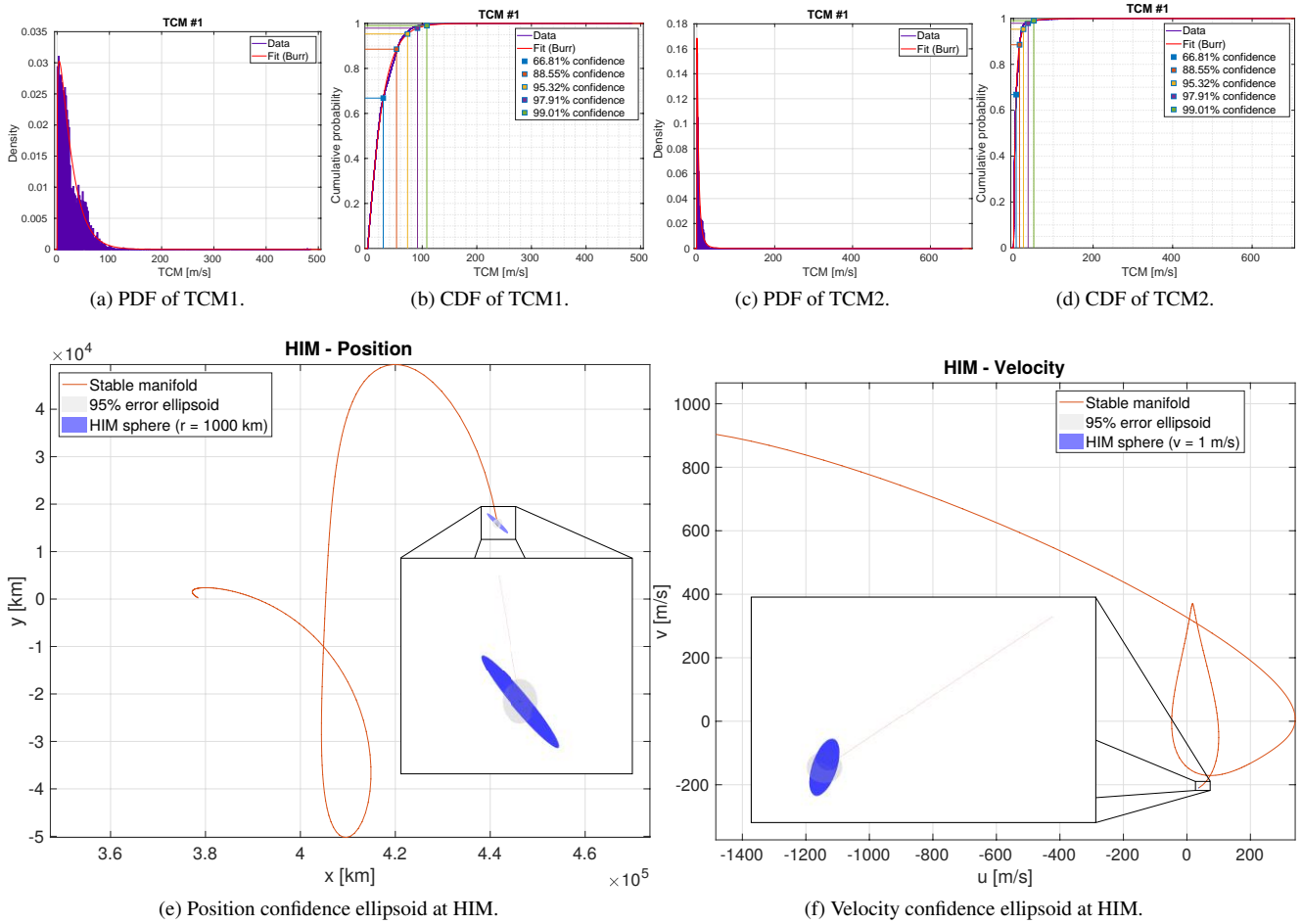(f) Velocity confidence ellipsoid at HIM.

Fig. 12: TCM.

and Figure 12d, respectively. Clearly, the first TCM is predominant, while the second adjusts the trajectory for a precise targeting of the halo injection point. Finally, Figure 12e and Figure 12f display the position and velocity ellipsoids, respectively, that ensure a 95% confidence level for the HIM targeting. Position and velocity trajectories from the SMIM to the HIM are also shown. The main axis of inertia of the confidence ellipsoid span $(277.2, 663.7, 3024.2)$ km in position $(0.69, 0.83, 2.65)$ m/s in velocity.

5 Baseline mission

5.1 Δv BUDGET

Mission Δv budgets for each maneuver and phase are reported in Table 8 with both deterministic and confidence values. The total 1σ-cost is 154.4 m/s, which is also in line with a 12U CubeSat volume and mass budgets.

5.2 TIME WINDOW FOR INJECTION INTO PARKING ORBIT

The time window for parking orbit insertion is selected solely based on constraints on autonomy of navigation. During the parking phase, LUMIO uses the Earth as celestial reference for optical navigation. To ensure a sufficient degree of performance of the camera and the filtering routine, at least 50% of the Earth visible part shall be illuminated for more than seven consecutive days. These constraints

Tab. 8: Mission Δv budgets.

Maneuver	Cost [m/s]			
	Deterministic	1σ	2σ	3σ
PCM	0	-	-	-
Transition orbit S/K	-	8	8	8
SMIM	89.47	-	-	-
TCM1	-	28.6	53.0	73.1
TCM2	-	6.5	15.0	24.8
HIM	0.5	-	-	-
1-year S/K	-	18.3	23.9	28.1
Disposal	3	-	-	-
TOTAL	154.4		192.9	227.0

translates into LUMIO–Earth–sun angles, as sketched in Figure 13, and thus into epochs. Specifically, there are 12 possible insertion windows during any year lasting approximately 7 days. Table 9 displays the injection date windows for the year 2023.

5.3 GRANULAR OPERATIONS

The period of the quasi-halo does not match the constant orbital period of its CRTBP counterpart, neither it matches the synodic period of the Earth–Moon system. Thus, the S/C orbiting the quasi-halo is not locked in a 2:1 resonance mechanism, rather it oscillates with varying amplitude around a nominal value, as shown in Figure 14.
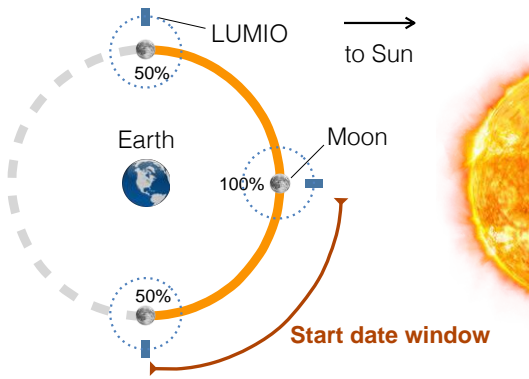
Fig. 13: Sketch of initial date selection.

Tab. 9: Initial dates.

Year 2023			
January	15 – 21	February	13 – 20
March	15 – 21	April	13 – 20
May	12 – 19	June	10 – 18
July	10 – 17	August	08 – 16
September	07 – 15	October	06 – 14
November	05 – 13	December	05 – 12

The regular and repetitive ConOps outlined in Section 4.1 has been used to plan and the S/K strategy (see Section 4.2). In the real-life application, the spacecraft would have to switch between Science and Nav&Eng orbits based on in-flight requirements and feasibility of operations. For example, during the Science orbit the spacecraft shall observe the lunar surface with the optical payload to meet the mission scientific goals and requirements. In order to increase the signal-to-noise ratio (SNR) of optical measurements, observations must be made with sufficient dark condition on the Moon farside. A threshold of 50% illumination is put to avoid stray light and saturation of the detector. On the other hand, one of the tasks LUMIO shall carry out during the Nav&Eng orbit is autonomous optical orbit determination, whose performances increase with the visible illuminated percentile of lunar surface.

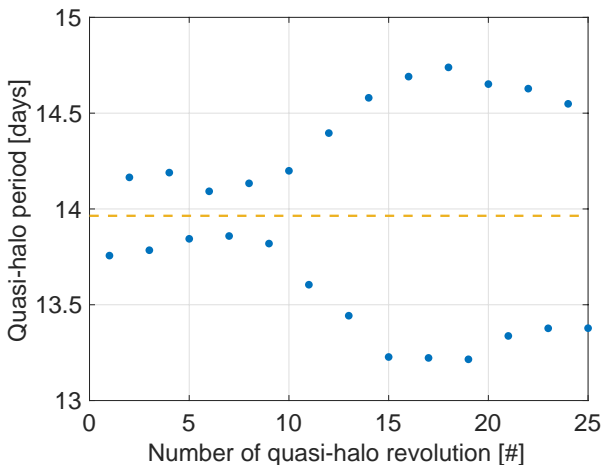A geometric constraint on the illuminated portion of the Moon farside is used to trigger operations switch between Science and Nav&Eng orbits, compatibly with the task LUMIO has to perform. The illumination condition depends on the mission initial epoch. In Figure 15, three timelines are shown: 1) the top line corresponds to a regular planning of ConOps, 2) the middle timeline represents the epoch-dependent ConOps when the geometric constraint on illumination of lunar farside is considered, and 3) the bottom timeline is the intersection between planning and geometry ConOps. Clearly, the duration of the Science orbits, according to the geometric analysis, experiences large deviations, always being lower than the assumed 14 days. The bottom timeline is interpreted as follows: if the flight dynamics team deems that the regular and repetitive features of the S/K strategy has to be preserved, then the windows in which Science or Nav&Eng tasks may be carried out are those highlighted in the bottom timeline of Figure 15.

Maximization of Science orbit duration leads to the selection of windows for possible mission starting dates. Figure 16 shows the effective days allocated to Science and Nav&Eng orbits. The worst deviations from the ideal scenario occurs across the spring equinox occurring on March 20 2023 at 21:25 GMT, that is roughly 115.5 days after the starting date for the parametric search. As a result, out of 182 days the best situation offers a Science of 82.2% and a Nav&Eng of 86.5% over a 1-year test case for nominal operative life, with the HIM planned on September 6 2023 and the parking orbit release window between August 8-16 2023. Table 10 shows a detailed timeline for the proposed LUMIO mission.

6 Conclusion

The primary science goal of LUMIO is to observe meteoroid impact flashes on the lunar farside in order to study the characteristics of meteoroids and to improve the meteoroid models of the solar system. This may lead to a further study of the sources of these meteoroids, such as asteroids in the near-Earth environment and comets. LUMIO complements ground-based observations with remote space-based observations, so improving the lunar situational awareness.

A baseline for LUMIO mission is proposed. An orthodox trade-off logic is followed, resulting in the selection of a Earth–Moon L_2 quasi-halo orbit as operative solution. Extensive Monte-Carlo simulations show the feasibility of the mission also in terms of trajectory correction maneuvers during the stable manifold transfer, and in terms of station-keeping cost during the Navigation and Engineering orbit. This allows for a pristine Science orbit and thus maximize the scientific return of the mission. The Δv budget of 227 m/s, at 3σ confidence, is within the capabilities of a CubeSat and in line with the deployment platform requirements.

Acknowledgments

Fig. 14: Quasi-halos period. Line is the period of the CRTBP halo.
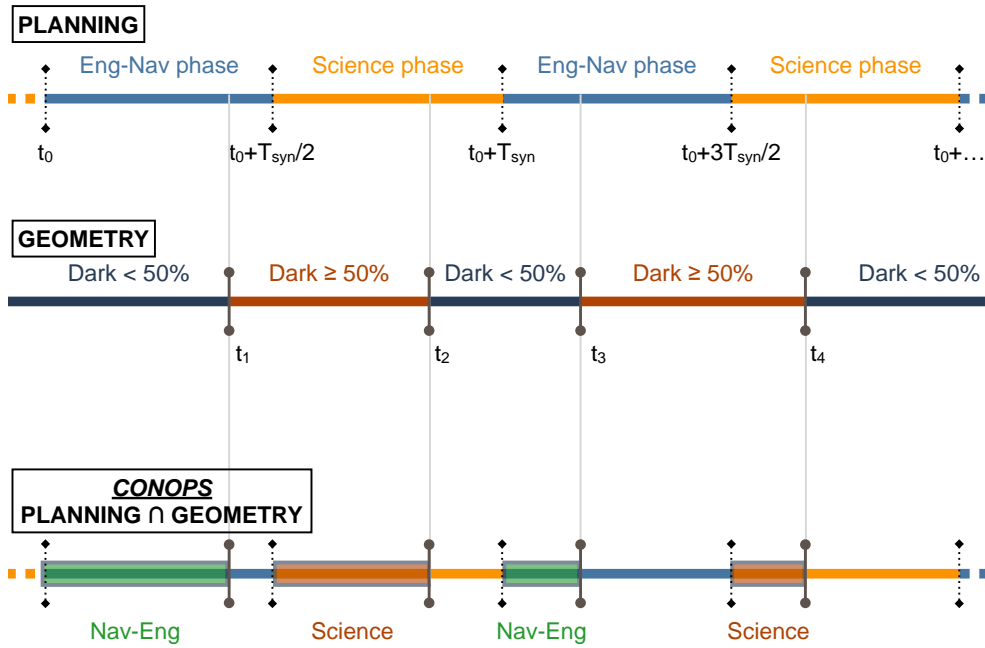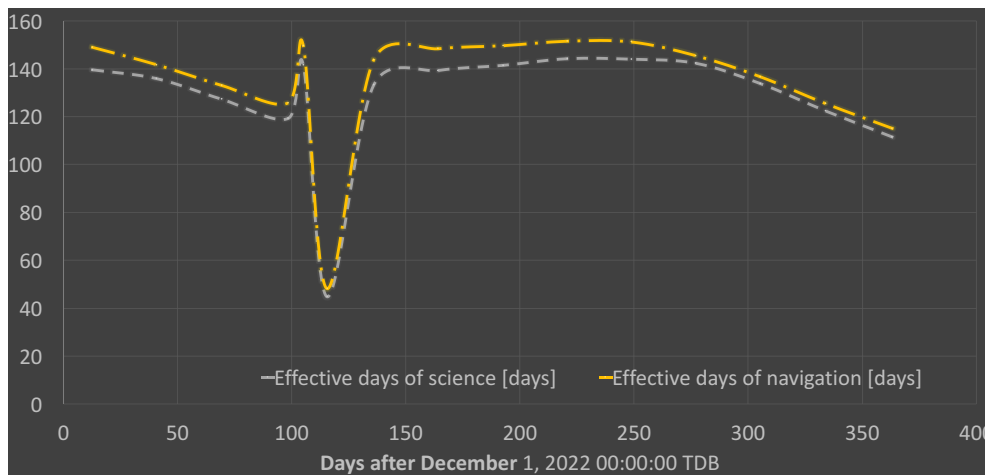
Fig. 15: Granularity of ConOps.

Fig. 16: Deviation of Science and Nav&Eng orbits from regular planning ConOps.

Tab. 10: LUMIO timeline.

Order	Date (2023)	Time	Task	Description
1	August 8-16	All day	LUMIO deployment	Lunar Orbiter injects LUMIO into selenocentric parking orbit.
2	August 23	00:00:00	SMIM	LUMIO maneuvers into the stable manifold of the target halo, starting the transfer phase.
3	August 24	00:00:00	TCM1	LUMIO performs the fisrt TCM.
4	August 30	00:00:00	TCM2	LUMIO performs the second TCM.
5	September 6	00:00:00	HIM	The HIM places LUMIO in the target operative halo orbit.
6	September 6	00:00:00	EoL	LUMIO executes a disposal maneuver and de-commissions its systems.

References

[1] J. Oberst, A. Christou, R. M. Suggs, D. E. Moser, I. Daubar, A. McEwen, M. Burchell, T. Kawamura, H. Hiesinger, K. Wünnemann, R. Wagner, and M. Robinson, "The present-day flux of large meteoroids on the lunar surface–a synthesis of models and observational techniques," *Planetary and Space Science*, vol. 74, no. 1, pp. 179–193, 2012. DOI: `10.1016/j.pss.2012.10.005`.

[2] E. Speyerer, R. Povilaitis, M. Robinson, P. Thomas, and R. Wagner, "Quantifying crater production and regolith overturn on the Moon with temporal imaging," *Nature*, vol. 538, no. 7624, pp. 215–218, 2016. DOI: `10.1038/nature19829`.

[3] A. M. Cipriano, D. A. Dei Tos, and F. Topputo, "Orbit design for LUMIO: The lunar meteoroid impacts observer," *Frontiers in Astronomy and Space Science*, vol. 5, no. 29, pp. 1–23, 2018. DOI: `10.3389/fspas.2018.00029`.

[4] E. Condoleo, C. Circi, and E. Ortore, "Constant orbit elements under the third body effect," *Advances in Space Research*, vol. 59, no. 5, pp. 1259–1269, 2017. DOI: `10.1016/j.asr.2016.11.035`.

[5] V. Franzese, P. Di Lizia, and F. Topputo, "Autonomous optical navigation for LUMIO mission," in *2018 Space Flight Mechanics Meeting, AIAA SciTech Forum (Kissimmee, FL: American Institute of Aeronautics and Astronautics))*, American Institute of Aeronautics and Astronautics, 2018, pp. 1–11. DOI: `10.2514/6.2018-1977`.

[6] D. Dei Tos and F. Topputo, "Trajectory refinement of three-body orbits in the real solar system model," *Advances in Space Research*, vol. 59, no. 8, pp. 2117–2132, 2017. DOI: `10.1016/j.asr.2017.01.039`.

[7] C. Acton Jr, "Ancillary data services of NASA's navigation and ancillary information facility," *Planetary and Space Science*, vol. 44, no. 1, pp. 65–70, 1996. DOI: `10.1016/0032-0633(95)00107-7`.

[8] C. Acton Jr, N. Bachman, B. Semenov, and E. Wright, "A look towards the future in the handling of space science mission geometry," *Planetary and Space Science*, vol. 150, pp. 9–12, 2018, ISSN: 0032-0633. DOI: `10.1016/j.pss.2017.02.013`.

[9] G. Mengali and A. Quarta, "Optimization of biimpulsive trajectories in the Earth-Moon restricted three-body system," *Journal of Guidance, Control, and Dynamics*, vol. 28, no. 2, pp. 209–216, 2005. DOI: `10.2514/1.7702`.

[10] N. Dwivedi, "Deterministic optimal maneuver strategy for multi-target missions," *Journal of Optimization Theory and Applications*, vol. 17, no. 1, pp. 133–153, Oct. 1975. DOI: `10.1007/BF00933919`.

[11] K. Howell and H. Pernicka, "Stationkeeping method for libration point trajectories," *Journal of Guidance Control and Dynamics*, vol. 16, pp. 151–151, 1993. DOI: `10.2514/3.11440`.

[12] K. Oguri, K. Kakihara, S. Campagnola, N. Ozaki, K. Ohima, T. Yamaguchi, and R. Funase, "EQUULEUS mission analysys: Design of the science orbit phase," in *26th International Symposium on Space Flight Dynamics (Ehime, Japan)*, 2017, pp. 1–7.

[13] D. Folta, T. Pavlak, A. Haapala, K. Howell, and M. Woodard, "Earth–moon libration point orbit stationkeeping: Theory, modeling, and operations," *Acta Astronautica*, vol. 94, no. 1, pp. 421–433, 2014. DOI: `10.1016/j.actaastro.2013.01.022`.

[14] F. Topputo, "Fast numerical approximation of invariant manifolds in the circular restricted three-body problem," *Communications in Nonlinear Science and Numerical Simulation*, vol. 32, no. Supplement C, pp. 89–98, 2016. DOI: `10.1016/j.cnsns.2015.08.004`.

[15] G. Gómez, A. Jorba, J. Masdemont, and C. Simó, "Study of the transfer from the earth to a halo orbit around the equilibrium point L1," *Celestial Mechanics and Dynamical Astronomy*, vol. 56, no. 4, pp. 541–562, Aug. 1993. DOI: `10.1007/BF00696185`.

[16] G. Gómez, J. Marcote, and J. Masdemont, "Trajectory correction manoeuvres in the transfer to libration point orbits," *Acta Astronautica*, vol. 56, no. 7, pp. 652–669, 2005. DOI: `10.1016/j.actaastro.2004.11.005`.

[17] R. Serban, W. Koon, M. Lo, J. Marsden, L. Petzold, S. Ross, and R. Wilson, "Halo orbit mission correction maneuvers using optimal control," *Automatica*, vol. 38, no. 4, pp. 571–583, 2002. DOI: `10.1016/S0005-1098(01)00279-5`.